Thermomechanical model for argillaceous hard soils - weak rocks: application to THM simulation of deep excavations in claystone

Saeed Tourchi*[1], Miguel A. Mánica[2], Jean Vaunat[3], and Antonio Gens[3]

[1]Institute of Hydrogeology, Engineering Geology and Applied Geophysics, Faculty of Science, Charles University, Prague, Czech Republic.

[2]Institute of Engineering, National Autonomous University of Mexico, Mexico City, Mexico.

[3]Department of Civil and Environmental Engineering, Universitat Politècnica de Catalunya, Barcelona Tech - CIMNE, Barcelona, Spain.

Abstract

The paper presents the enhancement of an existing constitutive model for argillaceous hard soils-weak rocks for non-isothermal conditions, to be used in coupled thermo-hydro-mechanical (THM) simulations of underground excavations subjected to temperature variations within the context of deep geological nuclear waste disposal. The proposed thermo-elastoplastic extension accounts for the effect of temperature on the yield and plastic potential functions, and on the elastic stiffness. The resulting model is validated through the simulation of relevant non-isothermal laboratory tests reported in the literature. The model is then applied to the coupled THM simulation of an in situ heating test conducted at the Meuse/Haute-Marne underground research laboratory, in Bure, France, excavated in the Callovo-Oxfordian claystone. Results show that the incorporation of thermal effects into the constitutive description of the host rock plays a significant role in the behaviour of the excavation when subjected to thermal loading, particularly in the evolution of the excavation damaged zone.

Keywords: claystone; constitutive modelling; elastoplasticity; thermal behaviour; underground excavations; THM analyses.

*Corresponding author: tourchis@natur.cuni.cz

Preprint submitted to EarthArXiv (non peer-reviewed).

1 Introduction

This contribution addresses the thermo-hydro-mechanical modelling of indurated argillaceous materials, i.e. geological materials where clay minerals predominate. They frequently occupy a transition zone where they can be either classified as hard soils or weak rocks, and they are widely distributed in nature representing up to 50% of the global sedimentary rock mass (Gens, 2013). The significant interest in these materials arises from the fact that they are being currently considered as potential host media for high and intermediate-level and long-lived nuclear waste. They provide advantageous features such as low permeability, a degree of self-healing capacity, and substantial retardation properties for solute transport (Gens, 2013; Armand et al., 2017). On the other hand, they are sensitive to chemical changes and, due to their relatively low strength, excavations often require support (Gens et al., 2007). In situ observations have also shown that excavation operations induce damage in these materials in the form of fracture networks (see e.g. Armand et al., 2014). The zone containing these fractures is usually known as the excavation damaged zone (EDZ), and it plays a major role in the hydromechanical behaviour of underground excavations (Mánica et al., 2022a,b).

Given the exothermic nature of radioactive waste, temperature increases will take place in the host rock around the disposal cells. Therefore, the potential effects of this thermal loading, particularly on the EDZ, are important aspects to consider in the performance assessment of deep geological repositories. The host rock, containing the exothermic waste canisters, will be exposed to various coupled mechanical, hydraulic, and thermal phenomena that can affect the near-field behaviour of excavations and the evolution of the EDZ. Therefore, proper understanding and modelling of nuclear waste repositories require the incorporation of those phenomena in the constitutive description of the host rock.

Several thermomechanical models that can reproduce most of the observed behaviour of saturated clays at elevated temperatures have been developed by several researchers. Hueckel and Borsetto (1990) developed one of the first models by extending the well-known Cam-Clay model to consider thermo-elastoplastic behaviour. Their proposed model encompasses shrinking the elastic domain during heating (thermal softening) and expanding during cooling when the stress path is within the yield surface. In fact, adopting similar assumptions, most subsequent models are based on the same principle (Robinet et al., 1996; Modaressi and Laloui, 1997; Cui et al., 2000; Graham et al., 2001; Abuel-Naga et al., 2009; Laloui and François, 2009; Yao, Y. and Zhou; Di Donna and Laloui, 2015; Hamidi et al., 2015; Tourchi and Hamidi, 2015; Zhou C and Ng CW., 2015; Hamidi et al., 2017; Hamidi and Tourchi, 2018; Maranha et al., 2018). In the meantime, the concept of bounding surface plasticity has also been extended to improve the modelling of cyclic behaviour at various temperatures and volume change under thermal loading at intermediately and highly overconsolidated states (Modaressi and Laloui, 1997; Laloui and Cekerevac, 2008; Laloui and François, 2009; Di Donna and Laloui, 2015; Zhou et al., 2017; Zhou and Ng, 2018; Cheng et al., 2020; Golchin et al., 2022a,b).

As noted in the previous paragraph, many of the thermomechanical formulated in the framework of critical state concept and modified Cam-clay, in which thermo-plastic behaviour is incorporated using a temperature-dependent yield pressure. The latter is particularly suitable for normally consolidated (or lightly overconsolidated) soft clays, where their behaviour is controlled, to a large extent, by a volumetric yielding mechanism. However, this is not necessarily the case for indurated argillaceous materials, where strong post-sedimentation diagenetic bonds make the mobilisation of the shear resistance more likely in typical engineering applications, including deep tunnelling. Therefore, from a practical standpoint, a Mohr-Coulomb type failure criterion can be demeaned adequate for characterising the behaviour of the stiff clayey materials considered as possible host mediums for deep geological disposal (Mánica et al., 2017). Nevertheless, as shown by experimental evidence (e.g. De Bruyn and Thimus, 1996; Zhang et al., 2007; Menaceur et al., 2015; Liu et al., 2019), strength and stiffness parameters are affected by temperature changes that might significantly affect the behaviour of excavations.

In this context, the aim of the work is to provide a thermomechanical model for argillaceous rocks, with emphasis on the deviatoric yielding mechanism, to be used in coupled thermo-hydro-mechanical (THM) simulations of underground excavations subjected to temperature variations. Particularly, the work involves the extension of the constitutive model from Mánica et al. (2017), hereafter called the reference model, to non-isothermal conditions. The reference model uses a Mohr-Coulomb yield criterion and incorporates a number of features that are considered relevant for the satisfactory description of indurated clayey materials, such as strength and stiffness anisotropy, nonlinear isotropic hardening/softening, time-dependent deformations, and the evolution of permeability with the accumulation of irreversible strains. The proposed thermo-elastoplastic extension accounts for the effect of temperature on the yield and plastic potential functions and on the elastic stiffness. The resulting model is validated through the simulation of relevant non-isothermal laboratory test results reported in the literature. The model is then applied to the coupled THM modelling of an in situ heating test (Bumbieler et al., 2021) carried out at the Meuse/Haute-Marne (MHM) underground research laboratory (URL), excavated in the Callovo Oxfordian (COx) claystone. This in situ experiment has already been simulated by Tourchi et al. (2021), using the isothermal version of the reference model. Although the previous results were satisfactory, it is shown here that the incorporation of thermal effects into the constitutive description of the host rock plays a significant role in the behaviour of the excavation when subjected to thermal loading, particularly in the evolution of the EDZ.

2 Thermomechanical behaviour of argillaceous rocks

Comprehensive experimental data exist on the thermomechanical behaviour of clayey soils. In general, heating saturated clays, under drained conditions, induces strength and volume

changes that depend on the stress history. Temperature-induced volume changes tend to be contractive and irreversible for normally consolidated clays whereas expansive and reversible deformations occur for highly overconsolidated clays (Campanella and Mitchell, 1968; Plum and Esrig, 1969; Baldi et al., 1988; Hueckel and Borsetto, 1990; Sultan et al., 2002; Cekerevac and Laloui, 2004; Abuel-Naga et al., 2006; Tsutsumi and Tanaka, 2012; Di Donna and Laloui, 2015; Shetty et al., 2019). However, experimental data on the thermomechanical behaviour of argillaceous rocks are scarce in the scientific literature (Zhang et al., 2007; Monfared et al., 2012; Zhang et al., 2014; Menaceur et al., 2015; Liu et al., 2019). In general, two main phenomena appear of major importance regarding the thermomechanical behaviour of argillaceous rocks: (1) continuous variation of mechanical properties (e.g. strength and stiffness parameters) with temperature, with a transition to a more ductile behaviour at elevated temperatures, and (2) temperature-induced reversible expansive strains followed, at some threshold temperature value, by irreversible contractive strains. These phenomena are further discussed in the following sections.

2.1 Temperature-induced changes in mechanical properties

De Bruyn and Thimus (1996) performed a number of isotropically consolidated undrained (CIU) triaxial tests at different temperatures on Boom clay samples (Figure 1a), a Tertiary plastic clay of modest cementation and relatively low strength. They show that heating up to about 80°C led to a considerable loss of the shear strength of the material. With respect to the thermal behaviour of stiffer argillaceous rocks, Zhang et al. (2007) observed in CIU triaxial tests on Opalinus clay samples that the peak deviatoric stress and the stiffness reduce with increasing temperature, showing an increasingly ductile behaviour (Figure 1b). Zhang et al. (2014) and Menaceur et al. (2015) (Figure 2a) confirmed these observations on COx claystone under drained conditions. More recently, Liu et al. (2019) conducted a series of pseudo-drained lateral decompression tests, at constant mean stress, on COx samples (Figure 2b). Again, a reduction of the strength is observed as temperature increases, confirming the temperature-driven strength evolution.

Figure 3 summarises the test results from Figures 1 and 2 in terms of the peak strength as a function of temperature. It can be observed that the peak deviatoric stress generally reduces monotonically with temperature, showing a similar trend in all test series. Of course, the actual peak values depend on the material, reflecting their different origin, diagenesis, and subsequent geological history, and on the loading path imposed by the tests performed. Boom clay samples show strengths about half an order of magnitude lower than COx and Opalinus clay samples. Nevertheless, results can be normalised with respect to the strength at a given reference temperature T_0. Figure 4 shows this normalisation in terms of $q_{\text{peak}}(T)/q_{\text{peak}}(T_0)$ vs. T/T_0, where $q_{\text{peak}}(T)$ is the peak deviatoric stress at a given temperature T and $q_{\text{peak}}(T_0)$ is the peak deviatoric stress at the reference temperature T_0, assumed here equal to the smallest

testing temperature. Although some dispersion is observed, from a practical standpoint we can characterise the dependence of the strength with temperature through the following expression:

$$q_{\text{peak}}(T) = q_{\text{peak}}(T_0)\left[1 - \mu_q \ln\left(T/T_0\right)\right] \tag{1}$$

where μ_q is a parameter controlling the rate of strength reduction. For instance, Figure 5 shows an example of the variation of the peak strength as a function of temperature according to Equation (1), for different values of μ_q. Although Equation (1) only refers to the variation of the peak deviatoric strength with temperature for specific conditions and stress paths, it can serve as the basis for defining the evolution laws of the yield envelope as a function of temperature for this indurated clayey materials, as it is done in Section 3.2.2.

As already mentioned, the stiffness also tends to reduce with temperature. For instance, Figure 6 shows the variation of Young's modulus E from the tests shown in Figures 1 and 2 in terms of $E(T)/E(T_0)$ vs. T/T_0, where $E\left(T_0\right)$ is Young's modulus at the reference temperature T_0 and $E\left(T\right)$ is the Young's modulus at a given temperature T. A similar behaviour is observed as in Figure 4 and, therefore, the variation of the E with temperature can be approximated with a similar logarithmic relationship than Equation (1):

$$E(T) = E(T_0)\left[1 - \mu_E \ln\left(T/T_0\right)\right] \tag{2}$$

where μ_E controls the rate of reduction of Young's modulus with temperature. Equations (1) and (2) are the basis for the proposed thermal extension of the reference model, described in Section 3.2.

2.2 Temperature-induced volumetric strains

Thermal volume changes in clays subjected to temperature elevation under constant stress depend on the degree of consolidation; thermo-elastic expansion and thermo-plastic contraction are observed for overconsolidated and normally consolidated clays respectively. However, as already mentioned, information is scarce for argillaceous indurated materials, such as those addressed in this work. For instance, in the case of COx claystone, Mohajerani et al. (2014) and Menaceur et al. (2015) first reported a contracting thermo-plastic behaviour, similar to that of normally consolidated clays. However, Zhang et al. (2017) later observed a thermal expansion behaviour in COx and Opalinus clay samples under different confinement pressures and different heating and cooling paths. More recent testing (Belmokhtar et al., 2017) also shows that indurated clayey materials first exhibit an elastic (reversible) thermal expansion, followed by a transition to a plastic thermal compression at some threshold temperature, as shown in Figure 7. The latter suggests that temperature might also affect the volumetric yielding mechanism of these materials, and the behaviour shown in Figure 7 could be incorporated here through a volumetric yielding cap that depends on temperature. Nevertheless, the present work focuses on the deviatoric yielding mechanism and, therefore, this expansion-contraction transition is not addressed here.

3 Thermomechanical constitutive model

3.1 Isothermal reference model (Mánica et al., 2017)

The reference model is implemented in terms of effective stresses, adopting the following generalised expression accounting for the effects of potential desaturation:

$$\boldsymbol{\sigma}' = \boldsymbol{\sigma} + S_{\mathrm{e}} s B \mathbf{I} \tag{3}$$

where $\boldsymbol{\sigma}'$ is the effective stress tensor, $\boldsymbol{\sigma}$ is the total stress tensor, S_{e} is the effective degree of saturation, s is the suction, B is the Biot's coefficient, and $\mathbf{I}$ is the identity tensor. The equivalent degree of saturation is given by the following form of the van Genuchten (1980) expression:

$$S_{\mathrm{e}} = \frac{S_l - S_{rl}}{S_{ls} - S_{rl}} = \left[1 + \left(\frac{p_g - p_l}{P}\right)^{\frac{1}{1-\lambda_{\mathrm{r}}}}\right]^{\lambda_{\mathrm{r}}} \tag{4}$$

where S_l is the degree of saturation, S_{lr} is the residual degree of saturation, S_{ls} is the degree of saturation in saturated conditions (normally 1), p_g and p_l are the gas and liquid pressures respectively, λ_{r} is a shape function coefficient, and P can be interpreted as the air-entry pressure value. In the following, the term *stress* always denotes effective stress and, therefore, the prime is dropped. Also, the soil mechanics sign convention if followed, i.e. compressive stress and strains are assumed positive.

The reference model comprises two main deformation mechanisms: (1) an instantaneous one related to the immediate deformations due to changes in effective stresses, and (2) a time-dependent one occurring under constant effective stress. Note that the instantaneous response also includes deformations caused by changes in effective stresses associated with consolidation (i.e. hydromechanical coupling). The instantaneous response is described within the framework of elastoplasticity, while for the time-dependent response an additional deformation mechanism is considered, following the plasticity-creep partition approach (Chaboche, 2008). Therefore, the strain decomposition assumed reads as follows:

$$d\boldsymbol{\epsilon} = d\boldsymbol{\epsilon}^{\mathrm{ep}} + d\boldsymbol{\epsilon}^{\mathrm{vp}} = d\boldsymbol{\epsilon}^{\mathrm{ep}} + dt\, \dot{\boldsymbol{\epsilon}}^{\mathrm{vp}} \tag{5}$$

where $d\boldsymbol{\epsilon}$ is the total strain increment; $d\boldsymbol{\epsilon}^{\mathrm{ep}}$ is the elastoplastic strain increment, related to the instantaneous response; $d\boldsymbol{\epsilon}^{\mathrm{vp}}$ is the viscoplastic strain increment, related to the time-dependent response; dt is the time increment, and $\dot{\boldsymbol{\epsilon}}^{\mathrm{vp}}$ is the viscoplastic strain rate tensor.

Under low deviatoric stresses, the response is linear elastic and characterised by a transversely isotropic (or cross-anisotropic) form of Hooke's law (see Wittke, 1990). For higher deviatoric stress, plastic deformations develop on reaching the yield surface, characterised by the Mohr-Coulomb criterion:

$$f = \left(\cos\theta + \frac{1}{\sqrt{3}} \sin\theta \sin\phi_{\mathrm{mob}}\right) J - \sin\phi_{\mathrm{mob}} \left(c_{\mathrm{mob}} \cot\phi_{\mathrm{mob}} + p\right) = 0 \tag{6}$$

where ϕ_{mob} is the mobilised friction angle, c_{mob} is the mobilised cohesion, and the remaining variables are stress invariants with their usual definition:

$$p = \frac{1}{3}\,\text{tr}\boldsymbol{\sigma} \tag{7}$$

$$J = \left(\frac{1}{2}\,\text{tr}\mathbf{s}^2\right)^{1/2} \tag{8}$$

$$\theta = -\frac{1}{3}\,\sin^{-1}\left(\frac{3\sqrt{3}\,\det\mathbf{s}}{2J^3}\right) \tag{9}$$

where $\mathbf{s} = \boldsymbol{\sigma} - p\mathbf{I}$ is the deviatoric stress tensor.

Hardening/softening is accounted for through the evolution of the strength parameters. The friction angle varies in a piecewise manner as follows:

$$\phi_{\text{mob}} = \begin{cases} \phi_{\text{ini}} + \dfrac{\epsilon^{\text{p}}_{\text{eq}}}{a_{\text{hard}} - \dfrac{\epsilon^{\text{p}}_{\text{eq}}\left(a_{\text{hard}} - \dfrac{\xi_1}{\phi_{\text{peak}} - \phi_{\text{ini}}}\right)}{\xi_1}} & \text{if } \epsilon^{\text{p}}_{\text{eq}} \leq \xi_1 \\ \phi_{\text{peak}} & \text{if } \xi_1 < \epsilon^{\text{p}}_{\text{eq}} \leq \xi_2 \\ \phi_{\text{peak}} - \dfrac{\epsilon^{\text{p}}_{\text{eq}} - \xi_2}{a_{\text{soft}} - \dfrac{\left(a_{\text{soft}} - \dfrac{\xi_3 - \xi_2}{\phi_{\text{peak}} - \phi_{\text{res}}}\right)\left(\epsilon^{\text{p}}_{\text{eq}} - \xi_2\right)}{\xi_3 - \xi_2}} & \text{if } \xi_2 < \epsilon^{\text{p}}_{\text{eq}} \leq \xi_3 \\ \phi_{\text{res}} & \text{if } \epsilon^{\text{p}}_{\text{eq}} > \xi_3 \end{cases} \tag{10}$$

where ϕ_{ini} is the initial friction angle, ϕ_{peak} is the peak friction angle, ϕ_{res} is the residual friction angle, $\epsilon^{\text{p}}_{\text{eq}}$ is the state variable controlling hardening/softening (Eq. 11), ξ_1 is the value of $\epsilon^{\text{p}}_{\text{eq}}$ at peak strength, ξ_2 is the value of $\epsilon^{\text{p}}_{\text{eq}}$ at which softening begins, ξ_3 is the value of $\epsilon^{\text{p}}_{\text{eq}}$ at which the residual strength is reached, a_{hard} is a parameter controlling the curvature of the function in the hardening branch, and a_{soft} is a parameter controlling the curvature of the function in the softening branch.

$$\epsilon^{\text{p}}_{\text{eq}} = \left(\frac{2}{3}\,\boldsymbol{\epsilon}^{\text{p}} : \boldsymbol{\epsilon}^{\text{p}}\right)^{1/2} \tag{11}$$

where $\boldsymbol{\epsilon}^{\text{p}}$ is the plastic strain tensor.

Cohesion evolves along with the friction angle, according to Equation (12), to allow the rotation of the Mohr-Coulomb envelope during hardening/softening, as shown in Figure 8.

$$c_{\text{mob}} = c_{\text{peak}}\cot\phi_{\text{peak}}\tan\phi_{\text{mob}} \tag{12}$$

where c_{peak} is the peak cohesion.

The model also accounts for strength cross-anisotropy (or transverse isotropy) through a non-uniform scaling of the stress tensor (Mánica et al., 2016). The latter approach is incorporated by replacing p, J, and θ, used to evaluate the yield condition (Equation 6), by p^{ani}, J^{ani}, and θ^{ani} respectively. These are invariants, with the same definition than Equations (7), (8), and (9), but computed from the anisotropic stress tensor $\boldsymbol{\sigma}^{\text{ani}}$, defined as:

$$\boldsymbol{\sigma}^{\text{ani}} = \begin{bmatrix} \dfrac{\sigma_{11}^r}{c_N} & c_S\sigma_{12}^r & \sigma_{13}^r \\ c_S\sigma_{12}^r & c_N\sigma_{22}^r & \sigma_{23}^r \\ \sigma_{13}^r & c_S\sigma_{23}^r & \dfrac{\sigma_{33}^r}{c_N} \end{bmatrix} \tag{13}$$

where c_N and c_S are the normal and shear scaling factors respectively, and σ_{ii}^r are the components of $\boldsymbol{\sigma}^r$. The latter corresponds to the stress tensor $\boldsymbol{\sigma}$, but oriented such that direction *2* is normal to the isotropic plane (i.e. normal to bedding in these sedimentary materials) via the usual rotation transformation. In this way, the yield surface is indirectly modified to account for cross-anisotropy. Further details on this approach, and on the physical meaning of the anisotropy parameters, can be consulted in Mánica et al. (2016).

Regarding the direction of plastic flow, a non-associated flow rule is adopted. Rather than derive a specific function for the plastic potential, the flow rule is directly obtained from the yield criterion in the following way:

$$\frac{\partial g}{\partial \boldsymbol{\sigma}} = \omega \frac{\partial f}{\partial p}\frac{\partial p}{\partial \boldsymbol{\sigma}} + \frac{\partial f}{\partial J}\frac{\partial J}{\partial \boldsymbol{\sigma}} + \frac{\partial f}{\partial \theta}\frac{\partial \theta}{\partial \boldsymbol{\sigma}} \tag{14}$$

where g is the plastic potential function and ω is a constant controlling the volumetric component of plastic deformations. With $\omega = 1$ an associated flow rule is recovered, while with $\omega = 0$ no volumetric plastic strains occur. An adequate value for geomaterials usually lies between these limits. However, it is important to notice that, due to the non-uniform scaling approach to incorporate strength anisotropy, f is defined in terms of the anisotropic stress invariants p^{ani}, J^{ani}, and θ^{ani}. Therefore, the flow rule can be computed as follow:

$$\frac{\partial g}{\partial \boldsymbol{\sigma}} = \omega \frac{\partial f}{\partial p^{\text{ani}}}\frac{\partial p^{\text{ani}}}{\partial \boldsymbol{\sigma}^{\text{ani}}}\frac{\partial \boldsymbol{\sigma}^{\text{ani}}}{\partial \boldsymbol{\sigma}} + \frac{\partial f}{\partial J^{\text{ani}}}\frac{\partial J^{\text{ani}}}{\partial \boldsymbol{\sigma}^{\text{ani}}}\frac{\partial \boldsymbol{\sigma}^{\text{ani}}}{\partial \boldsymbol{\sigma}} + \frac{\partial f}{\partial \theta^{\text{ani}}}\frac{\partial \theta^{\text{ani}}}{\partial \boldsymbol{\sigma}^{\text{ani}}}\frac{\partial \boldsymbol{\sigma}^{\text{ani}}}{\partial \boldsymbol{\sigma}} \tag{15}$$

where $\partial \boldsymbol{\sigma}^{\text{ani}}/\partial \boldsymbol{\sigma}$ is a Jacobian matrix containing the partial derivatives of the anisotropic stress components with respect to the global Cartesian stresses. In this way, the standard derivatives of the stress invariants are unchanged. $\partial \boldsymbol{\sigma}^{\text{ani}}/\partial \boldsymbol{\sigma}$ depends on the scaling factors C_N and C_S and on the orientation of the isotropic plane, and its definition can be found in Mánica et al. (2016). The same approach can be applied to compute the gradient of the yield function $\partial f/\partial \boldsymbol{\sigma}$, which is also required for the numerical implementation.

For the characterisation of the time-dependent deformation component, the strain rate tensor is computed as:

$$\dot{\boldsymbol{\epsilon}}^{\text{vp}} = \frac{2}{3}\frac{\dot{\epsilon}^{\text{vp}}}{q}\,\mathbf{s} \tag{16}$$

$$q = \left(\frac{3}{2} \mathbf{s} : \mathbf{s} \right)^{1/2} \tag{17}$$

$$\dot{\epsilon}^{\mathrm{vp}} = \gamma \left\langle q - \sigma_s \right\rangle^n \left(1 - \epsilon_{\mathrm{eq}}^{\mathrm{vp}} \right)^m \tag{18}$$

where γ is a viscosity parameter, σ_s is a threshold from which viscoplastic strains are activated, $\langle \cdot \rangle$ are the Macaulay brackets, n and m are material constants, and $\epsilon_{\mathrm{eq}}^{\mathrm{vp}}$ is the state variable of the time-dependent mechanism, given by:

$$\epsilon_{\mathrm{eq}}^{\mathrm{vp}} = \int_0^t \left(\frac{2}{3} \dot{\boldsymbol{\epsilon}}^{\mathrm{vp}} : \dot{\boldsymbol{\epsilon}}^{\mathrm{vp}} \right)^{1/2} dt \tag{19}$$

Finally, the model assumes that the intrinsic permeability evolves with plastic deformations to account for the observed permeability increase with damage in the COx claystone (see e.g. Armand et al., 2014). The plastic multiplier λ is used to characterise the magnitude of the accumulated plastic deformations, and the intrinsic permeability is defined by the following expression:

$$\mathbf{k} = \begin{cases} \mathbf{k} = \mathbf{k_0} \mathrm{e}^{\eta(\lambda - \lambda_0)} & \text{if } \lambda > \lambda_{\mathrm{thr}} \\ \mathbf{k_0} & \text{if } \lambda \leq \lambda_{\mathrm{thr}} \end{cases} \tag{20}$$

This model has been successfully employed to simulate the behaviour of underground excavations in COx claystone (e.g. Mánica et al., 2017; Gens et al., 2017; Alonso et al., 2021), and it was used to simulate the in situ heating tests addressed in this work (Tourchi et al., 2021). Nevertheless, as shown in Section 2, accounting for thermal effects on the constitutive description of the COx claystone plays a significant role when the host rock is subjected to thermal loading.

3.2 Thermomechanical extension

3.2.1 Thermo-elastic deformations

Assuming that the coefficient of thermal expansion is independent of stresses, the hypoelastic (incrementally reversible) strain increment can be defined as the sum of the thermal and mechanical components:

$$d\boldsymbol{\epsilon}^{\mathrm{e}} = d\boldsymbol{\epsilon}^{\mathrm{e},\boldsymbol{\sigma}} + \frac{1}{3} d\epsilon_v^{\mathrm{e},T} \, \mathbf{I} \tag{21}$$

where $d\boldsymbol{\epsilon}^{\mathrm{e},\boldsymbol{\sigma}}$ is the increment of elastic strains caused by changes in effective stresses and $d\epsilon_v^{\mathrm{e},T}$ is the elastic volumetric strain increment caused by changes in temperature T. The latter can be defined as:

$$d\epsilon_v^{\mathrm{e},T} = 3 b_s dT \tag{22}$$

where α_s is the linear thermal expansion coefficient of the medium, which depends on the material mineralogy, temperature, and pressure changes, although for practical purposes it can be assumed a constant.

On the other hand, as discussed in Section 2.1, the elastic stiffness, associated to $d\boldsymbol{\epsilon}^{\mathrm{e},\boldsymbol{\sigma}}$, is also affected by temperature. The latter is incorporated here through a dependence of the Young modulus E with temperature according to Equation (2). Since a transversely isotropic form of Hooke's low is being employed, Equation (2) is applied to the elastic constants E_1 (Young's modulus parallel to the isotropic plane), E_2 (Young modulus normal to the isotropic plane) and G_2 (shear modulus in planes normal to the isotropic plane), with the same μ_E value, while ν_1 (Poisson's ratio for the lateral strains due to loading parallel to the isotropic plane) and ν_2 (Poisson's ratio for the lateral strains due to loading normal to the isotropic plane) are assumed constant.

3.2.2 Thermo-plastic components

Key thermal effects in argillaceous rocks, at least in the context of geological disposal of radioactive waste, are those leading to plastic deformations and, therefore, those affecting the EDZ. As discussed in Section 2.1, the strength of these indurated clayey materials depends on temperature, showing a monotonic reduction as temperature increases. The latter implies that larger plastic deformations and a larger damaged zone can be expected under higher temperatures, as those induced by exothermic nuclear waste. Following, Hueckel and Borsetto (1990), this behaviour can be incorporated by assuming that the yield function depends also on temperature. Particularly, the adopted reference model is characterised by a Mohr-Coulomb yield function and, therefore, the dependence of the strength with temperature can be incorporated through the parameters ϕ and c. Since this effect must be included on top of the strength evolution due to mechanical loading (Equations 10 and 12), mobilised strength parameters must be a function of both plastic strains and temperature. In the case of the friction angle, Equation (1) can be adopted to define ϕ_{ini}, ϕ_{peak}, ϕ_{res} as a function of temperature in the following way:

$$\phi_{\mathrm{ini}}(T) = \phi_{\mathrm{ini}}^{T_0}\left[1 - \mu_\phi \ln\left(T/T_0\right)\right] \tag{23}$$

$$\phi_{\mathrm{peak}}(T) = \phi_{\mathrm{peak}}^{T_0}\left[1 - \mu_\phi \ln\left(T/T_0\right)\right] \tag{24}$$

$$\phi_{\mathrm{res}}(T) = \phi_{\mathrm{res}}^{T_0}\left[1 - \mu_\phi \ln\left(T/T_0\right)\right] \tag{25}$$

where $\phi_{\mathrm{ini}}^{T_0}$, $\phi_{\mathrm{peak}}^{T_0}$, and $\phi_{\mathrm{res}}^{T_0}$ are the initial, peak, and residual friction angles, respectively, at the reference temperature T_0, and μ_ϕ is a parameter controlling the rate of change of the friction angle with temperature. Figure 9 shows schematically the evolution of the friction angle, both as a function of plastic deformations ($\boldsymbol{\epsilon}_{\mathrm{eq}}^{\mathrm{p}}$) and temperature.

As in the case of mechanical loading, we assume that the Mohr-Coulomb envelope rotates around a fixed point and, therefore, we can define the temperature-dependent mobilised cohesion as:

$$c_{\mathrm{mob}}(T) = c_{\mathrm{peak}}^{T_0} \cot \phi_{\mathrm{peak}}^{\mathrm{T_0}} \tan \phi_{\mathrm{mob}}(T) \tag{26}$$

where $c_{\mathrm{peak}}^{T_0}$ is the peak cohesion at the reference temperature T_0.

The incorporated dependence of the yield function with temperature requires the modification of the standard form of Prager's consistency condition. In the case of plastic loading, the latter reads:

$$df = \frac{\partial f}{\partial \boldsymbol{\sigma}} d\boldsymbol{\sigma} + \frac{\partial f}{\partial \phi_{\text{mob}}} d\phi_{\text{mob}} = 0 \tag{27}$$

where

$$d\phi_{\text{mob}} = \frac{\partial \phi_{\text{mob}}}{\partial \epsilon^{\text{p}}_{\text{eq}}} \frac{\epsilon^{\text{p}}_{\text{eq}}}{\partial \boldsymbol{\epsilon}^{\text{p}}} d\boldsymbol{\epsilon}^{\text{p}} + \frac{\partial \phi_{\text{mob}}}{\partial T} dT \tag{28}$$

A term accounting for changes in the yield function due to changes in cohesion is omitted in Equation (27) because we are assuming here that c_{mob} is a function of ϕ_{mob} (Equation 26). Therefore, these changes are already contained in the second term of Equation 27. It is, of course, possible (in fact desired; see e.g. Mánica et al., 2022a) to define the cohesion independently from the friction angle. In the latter case, the additional term $(\partial f / \partial c_{\text{mob}})\, dc_{\text{mob}}$ must be included in Equation 27. The increment of plastic deformations $d\boldsymbol{\epsilon}^{\text{p}}$ is defined as:

$$d\boldsymbol{\epsilon}^{\text{p}} = d\lambda \frac{\partial g}{\partial \boldsymbol{\sigma}} \tag{29}$$

where λ is the plastic multiplier. By substituting Equation (29) into (27) and (28), we can define λ as:

$$d\lambda = \frac{1}{H} \left(\frac{\partial f}{\partial \boldsymbol{\sigma}} d\boldsymbol{\sigma} + \frac{\partial f}{\partial \phi_{\text{mob}}} \frac{\partial \phi_{\text{mob}}}{\partial T} dT \right) \tag{30}$$

where

$$H = -\frac{\partial f}{\partial \phi_{\text{mob}}} \frac{\partial \phi_{\text{mob}}}{\partial \epsilon^{\text{p}}_{\text{eq}}} \frac{\partial \epsilon^{\text{p}}_{\text{eq}}}{\partial \boldsymbol{\epsilon}^{\text{p}}} \frac{\partial g}{\partial \boldsymbol{\sigma}} \tag{31}$$

Therefore, plastic deformations are now also affected by the thermal variation of the strength parameters. Details on the loading/unloading conditions for thermomechanical paths, as well as the consequences of the thermal softening response for specific conditions, can be consulted in Hueckel and Borsetto (1990).

4 Model validation

In order to assess the presented thermomechanical extension of the reference model, a number of laboratory tests on COx samples, under different temperatures, were simulated. Particularly, the hollow cylinder triaxial tests from Menaceur et al. (2015) and the lateral decompression tests from Liu et al. (2019), shown in Figure 2, were considered for this modelling exercise. Obtained parameters, particularly those related to the thermal extension of the model, were later used in the simulation of the ALC1604 in situ heating test at the MHM URL. Simulations were performed from a constitutive standpoint, with a unit cube mesh and assuming a homogeneous stress/strain field. As reported in the experiments, drained conditions were considered. The latter hypothesis is much more likely to be fulfilled in the hollow cylinder triaxial tests from Menaceur et al. (2015), due to the small drainage length. However, even if fully drained conditions did not occur in the experiments, we are mainly interested here in the relative changes between the tests at different temperatures. Therefore, as long as the initial conditions of all

samples in each test series are similar, performed simulations can still provide an assessment of the proposed thermal extension of the reference model. Both test series were carried out with the major principal stress normal to bedding and, therefore, anisotropy does not play a role in the results. The latter is only partially true since the difference between Young's moduli normal and parallel to bedding does affect the lateral elastic expansion in the case of the decompression test from Liu et al. (2019). Nevertheless, this effect is small and, therefore, no anisotropy in either stiffness or strength was incorporated in the simulation of the tests. The time-dependent component was also not included and, therefore, the viscosity parameter γ was assumed equal to zero. Although these features are not relevant in these simulations, they are of utmost importance in the simulation of the in situ heating tests, described in Section 5.

Considered tests from Menaceur et al. (2015) were performed with initial mean effective stresses of 4 and 8 MPa and under temperatures of 25 and 80°C. All tests were isotropically consolidated up to an effective mean stress of 8 MPa (close to in situ conditions) under 25°C. Then, two of the tests were unloaded to $p_0 = 4$ MPa. In two tests, one for each confinement pressure, the temperature was increased up to 80°C, and the samples were then sheared under displacement control. The other two tests were shared, also under displacement control, at 25°C. Since the reference model does not include a volumetric yielding mechanism (cap), it is not necessary to reproduce the actual consolidation path followed and, therefore, the stress state and temperature before shearing were imposed as initial conditions in the simulations. Employed parameters are summarised in Table 1. They were selected to achieve a reasonable agreement with experimental results. It is important to notice that two different Young moduli were employed for the different consolidation pressures. The latter is due to the fact that results show a dependence of the stiffness with confinement that was not included in the simulation. Since the tests were performed at a constant temperature, thermal parameters such as the linear thermal expansion coefficient α_s, the thermal conductivity k_T, and the specific heat capacity c_s do not affect the results. They will be relevant for the simulation of the in situ heating tests (Section 5). On the other hand, the thermal parameters μ_E and μ_ϕ are those controlling the resulting stiffness and strength, respectively, for different temperatures, and they were calibrated to reproduce the observed behaviour. Simulation results are compared against laboratory data in Figure 10. It can be observed that the model was able to capture adequately the reduction of the stiffness and the strength when the temperature is increased from 25 to 80°C.

Considered tests from Liu et al. (2019) were consolidated isotropically to a mean effective stress of 12 MPa. The temperature was then increased at a rate of 20°C/h until reaching the target temperature for each test. Values of 20, 40, 60, 80, and 90°C were adopted. Again, the stress state and temperature were imposed in the simulation as initial conditions before shearing. After reaching the target temperature, samples were then shared by applying an axial displacement rate, resulting in a strain rate of 2E-6 s^{-1}, and simultaneously reducing the confinement pressure to achieve a constant mean effective stress path. However, the

simulation of this loading procedure is rather complicated, implying the reduction of lateral stresses at runtime as a function of the vertical reaction resulting from the applied vertical displacement rate. The mean effective stress path can be much more easily reproduced by controlling stresses both in the lateral and vertical directions. The drawback of the latter is that convergence is not possible beyond the peak strength, at the beginning of the softening regime. In any case, laboratory tests were halted just after the peak strength, or an unloading phase was performed close to the peak. Therefore, the stress-controlled alternative was considered adequate. Employed parameters are also shown in Table 1, and obtained results are compared against laboratory data in Figure 11. Again, the model was able to satisfactorily capture the strength and stiffness reduction observed as the temperature was increased from 20 to 90°C.

5 THM simulation of the ALC1604 in situ heating test

As previously mentioned, the ALC1604 in situ heating test, performed at the MHM URL, has already been simulated by Tourchi et al. (2021), using the reference model to characterise the host rock. Tourchi et al. (2021) performed two-dimensional (2D) and three-dimensional (3D) fully-coupled THM analyses to explain the observed behaviour, particularly the near-field response of the host rock due to the increase in temperature. In general, simulations were able to reproduce satisfactorily in situ observations. A particular outcome of the analyses is that the EDZ does not evolve significantly during the heating phase of the experiment; only a minor increase is observed as a result of creep and consolidation. However, the reference model assumes isothermal conditions and does not take into account the observed decrease of the strength and stiffness of the COx, and other indurated clayey materials, as temperature increases (see Section 2). Therefore, the mentioned analyses cannot assess the role of this feature of the clay rock in the behaviour of the excavation when subjected to thermal loading, particularly in the evolution of the EDZ. In this context, the present section describes a coupled THM simulation of the ALC1604 in situ heating test but using the thermal extension of the reference model, described in Section 3, to characterise the behaviour of the COx claystone.

5.1 Main features of the model

A THM 2D finite element (FE) analysis of the in situ heating tests was performed assuming plane strain conditions. Details on the adopted coupled THM numerical formulation can be consulted in Olivella et al. (1994). The same features and parameters as the 2D model reported in Tourchi et al. (2019a,b, 2021) were adopted here, which corresponds to a cross-section located 17.5 m into the tunnel, at the centre of Heater 3. However, unlike the mentioned work, the host rock is characterised here with the thermomechanical extension of the reference model, described in Section 3. Only a brief description of the implemented FE model is provided here. Further details can be found in Tourchi et al. (2021).

The model geometry and main boundary conditions are depicted in Figure 12. The dimension of the model is 50 x 50 m, and the 25 m from the microtunnel axis to the lateral boundary corresponds to the distance to the GRD gallery (see Figure 13). The mesh comprises 1408 quadrilateral elements and 1425 nodes, and it has been refined near the excavation in order to deal with the high temperature and pore pressure gradients in that zone. Null displacements were prescribed in the normal direction of all boundaries. A homogeneous anisotropic initial stress state was considered in the whole domain (i.e. gravity gradient was neglected), corresponding to the stresses determined at the main level of the MHM URL (-490 m) (Wileveau et al., 2007). An initial hydrostatic pore-water pressure distribution was assumed, and prescribed as a boundary condition, which results in a value of 4.7 MPa at the tunnel axis. The latter value corresponds to the one estimated at this elevation, unaffected by excavation works (Armand et al., 2013, 2014). Regarding thermal conditions, an initial temperature of 21.8°C has been assumed throughout the geometry, and it has been prescribed in all boundaries except for the position of the GRD gallery. Although the latter was not explicitly included in the simulation, the observed variations of temperature and pore pressures were prescribed as boundary conditions at this location. The excavation diameter is about 0.7 m, whereas the diameter of the casing is smaller, about 0.62 m. The heater rests on the excavation floor, resulting in an annular space of varying thickness between the casing and the COx, which will eventually be closed due to the convergence of the rock. Both the casing and the annular space were explicitly included in the simulation (Figure 12); the former was characterised by a linear elastic material and the latter by a bilinear material, accounting for the gap closure. More details can be consulted in Tourchi et al. (2021). In the excavation boundary, a liquid pressure of -0.1 MPa was prescribed after excavation to represent the ventilation process. Heat power was applied as a thermal flux in the microtunnel. 90% of the heat power was applied uniformly in the zone of the heaters, while the remaining 10% was applied in the air-filled annular space between the heater and the lining, in order to approximately reproduce the effects of radiation and air thermal convection. The partition of the total heat flux was calibrated based on the temperature observations.

A number of boreholes were drilled from the GAN and NRD galleries (Figure 13), where several measurement devices were installed, including temperature sensors and piezometers. Figure 14 shows the location of the observation points, contained in the analysis section, that are used for comparison with the simulation results.

Tables 3 and 4 show the parameters adopted for the COx claystone, relevant for the coupled THM simulation performed. All parameters correspond to those employed in Tourchi et al. (2021), except for μ_ϕ and μ_E, controlling the evolution of the strength and the stiffness with temperature, selected based on the simulation of the non-isothermal tests on COx samples described in Section 4. Employed parameters for the casing and the annular space are shown in tables 5 and 6 respectively, which also coincide with those adopted in Tourchi et al. (2021).

5.2 Obtained results

Figure 15 shows the resulting temperature field (a) at the end of heating and (b) at the end of the second cooling phase. A maximum temperature of about 85°C was reached in the vicinity of the excavation, which decreases to about 45°C at the end of cooling. The anisotropic response of the heat flux is evident in the temperature field, extending slightly more in the horizontal than in the vertical direction. The latter is the result of the assumed higher thermal conductivity parallel to bedding, compared to the value normal to bedding (Gens et al., 2007). Figure 16 shows the observed and computed evolution of temperature at the sensors indicated in Figure 14. The figure also shows the results obtained by Tourchi et al. (2021), using the isothermal version of the reference model. Although, in general, the results satisfactorily reproduced the observed behaviour, the importance of the heat dissipation in the direction normal to the analysis section has already been demonstrated by Tourchi et al. (2021), and better results can be obtained with a 3D analysis. Nevertheless, it is important to notice that quite similar results are obtained with the isothermal and non-isothermal versions of the reference model. The latter is due to the fact that the hydraulic and mechanical responses of the claystone do not significantly affect the thermal behaviour (Gens et al., 2007).

The resulting EDZ (a) at the end of the excavation and (b) at the end of the heating phase is shown in Figure 17 in terms of the cumulative value of the plastic multiplier, which is directly related to the magnitude of irreversible plastic strains and, therefore, is related to the degree of damage experienced by the host rock surrounding the excavation. The drift for the ALC1604 experiment is aligned parallel to the major horizontal stress σ_{H} and, therefore, there is a nearly isotropic initial stress state in planes normal to the tunnel axis (see Figure 12). However, the EDZ extend further in the horizontal direction for tunnels with this orientation (Armand et al., 2014), suggesting the anisotropic characteristics of the rock mass. This behaviour can be explained by including strength anisotropy in the constitutive description (Mánica et al., 2016, 2017, 2022a,b), as it is done in the reference model (see section 3.1). Therefore, the resulting contours of the plastic multiplier resemble nicely the observed configuration of the EDZ for tunnels with this orientation. The same satisfactory results were obtained by Tourchi et al. (2021), using the isothermal version of the model. However, in contrast to what is reported by Tourchi et al. (2021), the EDZ shows a significant evolution during the heating stage (Figure 17b). The latter can be more easily identified in Figure 18, showing the resulting cumulative value of the plastic multiplier, along a horizontal line from the tunnel wall, for the simulations using the isothermal and non-isothermal versions of the reference model; the simulation with the non-isothermal model results in a larger extension of the EDZ. The latter occurs because as temperature increases, the strength and stiffness of the material decrease, generating additional damage and accumulation of plastic deformations.

The development of the EDZ during heating can be further explored in Figure 19, showing the evolution of the plastic multiplier, at the locations indicated in Figure 14, both with the isothermal and non-isothermal versions of the constitutive model. Only at p_01, the plastic

multiplier shows a significant evolution with the isothermal model. At p_02, only a slight increase is identified, and at the remaining locations no additional plastic deformations occur in the claystone. On the other hand, all locations experienced additional plastic straining during heating with the non-isothermal model, as a result of the evolution of mechanical parameters with temperature.

To the best knowledge of the authors, there were no direct in situ measurement to assess the evolution of the EDZ after heating to validate the results obtained from the analysis. However, as demonstrated by Mánica et al. (2022a,b), the EDZ plays a major role in the behaviour of pore-water pressures in the host rock. Particularly, the increase of permeability due to damage significantly modifies the steady-state pore-water pressure distribution. Therefore, the behaviour of pore pressures can be employed to indirectly assess the computed evolution of the EDZ with the non-isothermal model.

Figure 20 shows the pore-water pressures at the locations indicated in Figure 14. In the piezometers approximately aligned with the horizontal direction (pre_1616 and pre_4001), there is an increase of the pressure as the excavation front approaches the analyses section, while in the vertical direction (pre_1617) the pressure is reduced. The latter is the result of the anisotropic deconfinement brought about by the anisotropic stiffness of the COx (see Mánica et al., 2022a, for further details). Then, after the front reaches the analysis section, the pressure at pre_1616 and pre_4001 drops rapidly due to the pressure gradient generated by the new hydraulic boundary condition, enhanced by the permeability increase due to damage. However, when heating begins the pressure increases sharply due to the thermal pressurisation of water, caused by the differential thermal expansion of the liquid and solid phases. Nevertheless, consolidation (i.e. the dissipation of excess pore-water pressures) occurs simultaneously, acting as a competing phenomenon. When the rate of increase of temperature decreases (see Figure 16), as the temperature field approaches steady-state conditions, consolidation starts to dominate causing the reduction of pore pressures. In general, both simulations, with the isothermal and non-isothermal models, reasonably capture the evolution of water pressures during the experiment. Nevertheless, results with the non-isothermal model are significantly closer to field values when consolidation dominates the pore-water pressure behaviour. The latter is the result of a larger extension of the EDZ (see Figure 18), causing the permeability increase with damage (Equation (20)) to occur further into the claystone, resulting in lower pressures that are more consistent with field values. These observations suggest that the evolution of mechanical parameters with temperature might result in some limited enlargement of the EDZ during heating.

6 Concluding remarks

This paper presents the enhancement of an existing constitutive model for the coupled THM simulation of deep excavations in argillaceous rocks subjected to thermal loading. The original

model includes a number of features that are relevant for the satisfactory description of these indurated clayey materials, such as strength and stiffness anisotropy, nonlinear isotropic hardening/softening, time-dependent deformations, and the evolution of permeability with damage. The non-isothermal extension is obtained by accounting for the observed evolution of mechanical (strength and stiffness) parameters with temperature. The model focuses on the deviatoric yielding mechanism, which is characterised by a Mohr-Coulomb criterion. Therefore, the effect of temperature on the strength is incorporated through the evolution of the friction angle and the cohesion with temperature.

The resulting thermomechanical model was validated through the simulation of relevant non-isothermal laboratory tests on COx argillite from the literature. The model was then applied to the 2D simulation of an in situ heating test at the MHM URL. Results were compared to in situ measurements and to the results obtained in previous simulations using the isothermal version of the model (Tourchi et al., 2021). It is shown that both the isothermal and non-isothermal versions reproduce satisfactorily the main trends of behaviour in terms of the configuration and extension of the EDZ, and the evolution of temperature and pore-water pressure around the excavation, in the host rock. However, the non-isothermal model results in a larger evolution of the EDZ during the heating phase of the experiment. The latter results in a larger zone where the permeability increase due to damage takes place and, therefore, in lower water pressures that are more consistent with field values. These results show that the incorporation of thermal effects into the constitutive description of the host rocks plays a significant role in the behaviour of the excavation when subjected to thermal loading.

Acknowledgments

this is the acknowledgements.

References

Abuel-Naga, H. M., Bergado, D. T., Bouazza, A., and Pender, M. (2009). Thermomechanical model for saturated clays. *Géotechnique*, 59(3):273–278.

Abuel-Naga, H. M., Bergado, D. T., Ramana, G. V., Grino, L., Rujivipat, P., and Thet, Y. (2006). Experimental evaluation of engineering behavior of soft bangkok clay under elevated temperature. *Journal of Geotechnical and Geoenvironmental Engineering*, 132(7):902–910.

Alonso, M., Vaunat, J., Vu, M.-N., Gens, A., and Mánica, M. A. (2021). Performance of large diameter storage structures in deep exothermic waste repository. In *9th International Conference on Computational Methods for Coupled Problems in Science and Engineering*, Online. ECCOMAS.

Armand, G., Conil, N., Talandier, J., and Seyedi, D. M. (2017). Fundamental aspects of the hydromechanical behaviour of Callovo-Oxfordian claystone: From experimental studies to model calibration and validation. *Computers and Geotechnics*, 85:277–286.

Armand, G., Leveau, F., Nussbaum, C., de La Vaissiere, R., Noiret, A., Jaeggi, D., Landrein, P., and Righini, C. (2014). Geometry and properties of the excavation-induced fractures at the Meuse/Haute-Marne URL drifts. *Rock Mechanics and Rock Engineering*, 47(1):21–41.

Armand, G., Noiret, A., Zghondi, J., and Seyedi, D. M. (2013). Short- and long-term behaviors of drifts in the Callovo-Oxfordian claystone at the Meuse/Haute-Marne Underground Research Laboratory. *Journal of Rock Mechanics and Geotechnical Engineering*, 5(3):221–230.

Baldi, G., Hueckel, T., and Pellegrini, R. (1988). Thermal volume changes of the mineral–water system in low-porosity clay soils. *Canadian Geotechnical Journal*, 25(4):807–825.

Belmokhtar, M., Delage, P., Ghabezloo, S., and Conil, N. (2017). Thermal Volume Changes and Creep in the Callovo-Oxfordian Claystone. *Rock Mechanics and Rock Engineering*, 50(9):2297–2309.

Bumbieler, F., Plúa, C., Tourchi, S., Vu, M. N., Vaunat, J., Gens, A., and Armand, G. (2021). Feasibility of constructing a full-scale radioactive high-level waste disposal cell and characterization of its thermo-hydro-mechanical behavior. *International Journal of Rock Mechanics and Mining Sciences*, 137(October 2020).

Campanella, R. G. and Mitchell, J. K. (1968). Influence of temperature variations on soil behavior. *Journal of the Soil Mechanics and Foundations Division*, 94(3):709–734.

Cekerevac, C. and Laloui, L. (2004). Experimental study of thermal effects on the mechanical behaviour of a clay. *International Journal for Numerical and Analytical Methods in Geomechanics*, 28(3):209–228.

Chaboche, J. L. (2008). A review of some plasticity and viscoplasticity constitutive theories. *International Journal of Plasticity*, 24(10):1642–1693.

Cheng, W., Chen, R., Hong, P., Cui, Y. and Pereira, J. (2020). A two-surface thermomechanical plasticity model considering thermal cyclic behavior. *Acta Geotechnica*, 15(10):2741–2755.

Cui, Y. J., Sultan, N., and Delage, P. (2000). A thermomechanical model for saturated clays. *Canadian Geotechnical Journal*, 37(3):607–620.

De Bruyn, D. and Thimus, J. F. (1996). The influence of temperature on mechanical characteristics of boom clay: The results of an initial laboratory programme. *Engineering Geology*, 41(1-4 SPEC. ISS.):117–126.

Di Donna, A. and Laloui, L. (2015). Response of soil subjected to thermal cyclic loading: Experimental and constitutive study. *Engineering Geology*, 190:65–76.

Gens, A. (2013). On the hydromechanical behaviour of argillaceous hard soils-weak rocks. In Anagnostopoulos, A., Pachakis, M., and Tsatsanifos, C., editors, *Proceedings of the 15th European Conference on Soil Mechanics and Geotechnical Engineering - Geotechnics of Hard Soils - Weak Rocks*, volume 4, pages 71–118, Athens. IOS Press.

Gens, A., Manica, M., Vaunat, J., and Ruiz, D. F. (2017). Modelling the Mechanical Behaviour of Callovo-Oxfordian Argillite. Formulation and Application. In Ferrari, A. and Laloui, L., editors, *Advances in Laboratory Testing and Modelling of Soils and Shales (ATMSS)*, pages 37–44, Villars-sur-Ollon. Springer.

Gens, A., Vaunat, J., Garitte, B., and Wileveau, Y. (2007). In situ behaviour of a stiff layered clay subject to thermal loading: observations and interpretation. *Géotechnique*, 57(2):207–228.

Golchin, A., Vardon, P. and Hicks, M. A. (2022). A thermodynamically consistent two surface/bubble thermo-mechanical model considering thermal and mechanical cyclic behaviour of fine-grained soils. *International Journal Of Solids And Structures*, 254:111847.

Golchin, A., Vardon, P. and Hicks, M. (2022). A thermo-mechanical constitutive model for fine-grained soils based on thermodynamics. *International Journal Of Engineering Science*, 174:103579.

Graham, J., Tanaka, N., Crilly, T., and Alfaro, M. (2001). Modified Cam-Clay modelling of temperature effects in clays. *Canadian Geotechnical Journal*, 38(3):608–621.

Hamidi, A., Tourchi, S. and Khazaei, C. (2015) Thermomechanical constitutive model for saturated clays based on critical state theory. *International Journal Of Geomechanics*, 64(2-3):135–145.

Hamidi, A., Tourchi, S. and Kardooni, F. (2017) A critical state based thermo-elasto-plastic constitutive model for structured clays. *Journal Of Rock Mechanics And Geotechnical Engineering*, 9(6):094–1103.

Hamidi, A. and Tourchi, S. (2018) A thermomechanical constitutive model for unsaturated clays. *International Journal Of Geotechnical Engineering*, 12(2):185–199.

Hueckel, T., François, B., and Laloui, L. (2009). Explaining thermal failure in saturated clays. *Géotechnique*, 59(3):197–212.

Hueckel, T. and Borsetto, M. (1990). Thermoplasticity of saturated soils and shales: Constitutive equations. *Journal of Geotechnical Engineering*, 116(12):1765–1777.

Laloui, L. and Cekerevac, C. (2003). Thermo-plasticity of clays: An isotropic yield mechanism. *Computers and Geotechnics*, 30(8):649–660.

Laloui, L and Cekerevac, C. (2008) Non-isothermal plasticity model for cyclic behaviour of soils. *International journal for numerical and analytical methods in geomechanics*, 32(5): 437–460.

Laloui, L. and François, B. (2009) ACMEG-T: A soil thermo-plasticity model. *Journal Of Engineering Mechanics*, 135(9).

Liu, Z., Shao, J., Xie, S., Conil, N., and Talandier, J. (2019). Mechanical Behavior of Claystone in Lateral Decompression Test and Thermal Effect. *Rock Mechanics and Rock Engineering*, 52(2):321–334.

Mánica, M., Gens, A., Vaunat, J., and Ruiz, D. F. (2017). A time-dependent anisotropic model for argillaceous rocks. Application to an underground excavation in Callovo-Oxfordian claystone. *Computers and Geotechnics*, 85:341–350.

Mánica, M. A., Gens, A., Vaunat, J., Armand, G., and Vu, M. N. (2022a). Numerical simulation of underground excavations in an indurated clay using non-local regularisation. Part 1: Formulation and base case. *Geotechnique*, 72(12):1092–112.

Mánica, M. A., Gens, A., Vaunat, J., Armand, G., and Vu, M. N. (2022b). Numerical simulation of underground excavations in an indurated clay using non-local regularisation. Part 2: sensitivity analysis. *Géotechnique*, 72(12):1113–1128.

Mánica, M. A., Gens, A., Vaunat, J., and Ruiz, D. F. (2016). A cross-anisotropic formulation for elasto-plastic models. *Géotechnique Letters*, 6(2):156–162.

Maranha, J., Pereira, C. and Vieira, A. (2018). Improved subloading thermo-viscoplastic model for soil under strictly isotropic conditions. *Geomechanics For Energy And The Environment*, 14:38–47.

Menaceur, H., Delage, P., Tang, A. M., and Conil, N. (2015). The thermomechanical behaviour of the Callovo-Oxfordian claystone. *International Journal of Rock Mechanics and Mining Sciences*, 78:290–303.

Modaressi, H. and Laloui, L. (1997). A thermo-viscoplastic constitutive model for clays. *International Journal for Numerical and Analytical Methods in Geomechanics*, 21(5):313–335.

Mohajerani, M., Delage, P., Sulem, J., Monfared, M., Tang, A. M., and Gatmiri, B. (2014). The thermal volume changes of the callovo-oxfordian claystone. *Rock Mechanics and Rock Engineering*, 47(1):131–142.

Monfared, M., Sulem, J., Delage, P., and Mohajerani, M. (2012). On the THM behaviour of a sheared Boom clay sample: Application to the behaviour and sealing properties of the EDZ. *Engineering Geology*, 124:47–58.

Olivella, S., Carrera, J., Gens, A., and Alonso, E. E. (1994). Non-isothermal multiphase flow of brine and gas through saline media. *Transport in Porous Media*, 15(3):271–293.

Plum, R. L. and Esrig, M. I. (1969). Some temperature effects on soil compressibility and pore pressure. Technical report, Issue103, Highway Research Board.

Robinet, J.-C., Rahbaoui, A., Plas, F., and Lebon, P. (1996). A constitutive thermomechanical model for saturated clays. *Engineering Geology*, 41(1):145–169.

Shetty, R., Singh, D. N., and Ferrari, A. (2019). Volume change characteristics of fine-grained soils due to sequential thermomechanical stresses. *Engineering Geology*, 253(March):47–54.

Sultan, N., Delage, P., and Cui, Y. J. (2002). Temperature effects on the volume change behaviour of Boom clay. *Engineering Geology*, 64(2-3):135–145.

Tourchi, S. and Hamidi, A. (2015) Thermo-mechanical constitutive modeling of unsaturated clays based on the critical state concepts. . *Journal Of Rock Mechanics And Geotechnical Engineering* , 7(2):193–198.

Tourchi, S., Vaunat, J., Gens Solé, A., Vu, M.N. and Bumbieler, F., (2019). Thermo-hydro-mechanical simulation of a full-scale steel-lined micro-tunnel excavated in the callovooxfordian claystone. In *COMPLAS XV: proceedings of the XV International Conference on Computational Plasticity: fundamentals and applications*, volume 205, page 544-552. International Centre for Numerical Methods in Engineering (CIMNE).

Tourchi, S., Vaunat, J., Gens Solé, A., Vu, M.N. and Bumbieler, F., (2019). Coupled THM analysis of long-term anisotropic convergence in the full-scale micro tunnel excavated in the Callovo-Oxfordian argillite. In *VIII International Conference on Computational Methods for Coupled Problems in Science and Engineering: COUPLED 2019*, page 292-299. International Centre for Numerical Methods in Engineering (CIMNE).

Tourchi, S., Gens, A., Vaunat, J., Mánica, M. A., and Scaringi, G. (2020). A thermomechanical model for argillaceous rocks. In *2nd internacional conference on energy geotechnics*, volume 205, page 13014. E3S Web of Conferences.

Tourchi, S., Vaunat, J., Gens, A., Bumbieler, F., Vu, M. N., and Armand, G. (2021). A full-scale in situ heating test in Callovo-Oxfordian claystone: observations, analysis and interpretation. *Computers and Geotechnics*, 133(February).

Tsutsumi, A. and Tanaka, H. (2012). Combined effects of strain rate and temperature on consolidation behavior of clayey soils. *Soils and Foundations*, 52(2):207–215.

van Genuchten, M. T. (1980). A closed-form equation for predicting the hydraulic conductivity of unsaturated soils. *Soil Science Society of America Journal*, 44(5):892–898.

Wileveau, Y., Cornet, F. H., Desroches, J., and Blumling, P. (2007). Complete in situ stress determination in an argillite sedimentary formation. *Physics and Chemistry of the Earth*, 32(8-14):866–878.

Wittke, W. (1990). *Rock mechanics: theory and applications with case histories*. Springer-Verlag Berlin Heidelberg.

Yao, Y. and Zhou, A. (2013) Non-isothermal unified hardening model: a thermo-elasto-plastic model for clays. *Géotechnique*. 63(15):1328–45.

Zhang, C. L., Conil, N., and Armand, G. (2017). Thermal effects on clay rocks for deep disposal of high-level radioactive waste. *Journal of Rock Mechanics and Geotechnical Engineering*, 9(3):463–478.

Zhang, C. L., Rothfuchs, T., Su, K., and Hoteit, N. (2007). Experimental study of the thermo-hydro-mechanical behaviour of indurated clays. *Physics and Chemistry of the Earth*, 32(8-14):957–965.

Zhang, F., Hu, D. W., Xie, S. Y., and Shao, J. F. (2014). Influences of temperature and water content on mechanical property of argillite. *European Journal of Environmental and Civil Engineering*, 18(2):173–189.

Zhou, C. and Ng, C. (2015). A thermomechanical model for saturated soil at small and large strains. *Canadian Geotechnical Journal*, 52(8):1101–1110.

Zhou, C., Fong, K. and Ng, C. (2017). A new bounding surface model for thermal cyclic behaviour. *International Journal For Numerical And Analytical Methods In Geomechanics*. 41(16):1656–1666

Zhou, C. and Ng, C. (2018). A new thermo-mechanical model for structured soil. *Géotechnique* 68(12):1109–1115

Figures

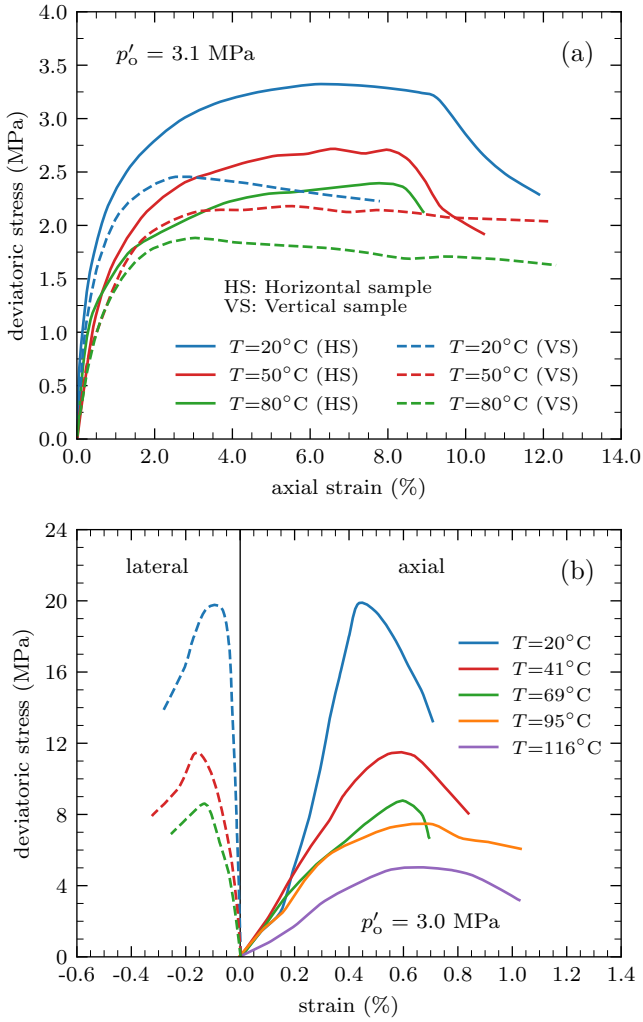

Figure 1: Results of CIU triaxial test at different temperatures on (a) Boom clay (De Bruyn and Thimus, 1996) and (b) Opalinus clay (Zhang et al., 2007).

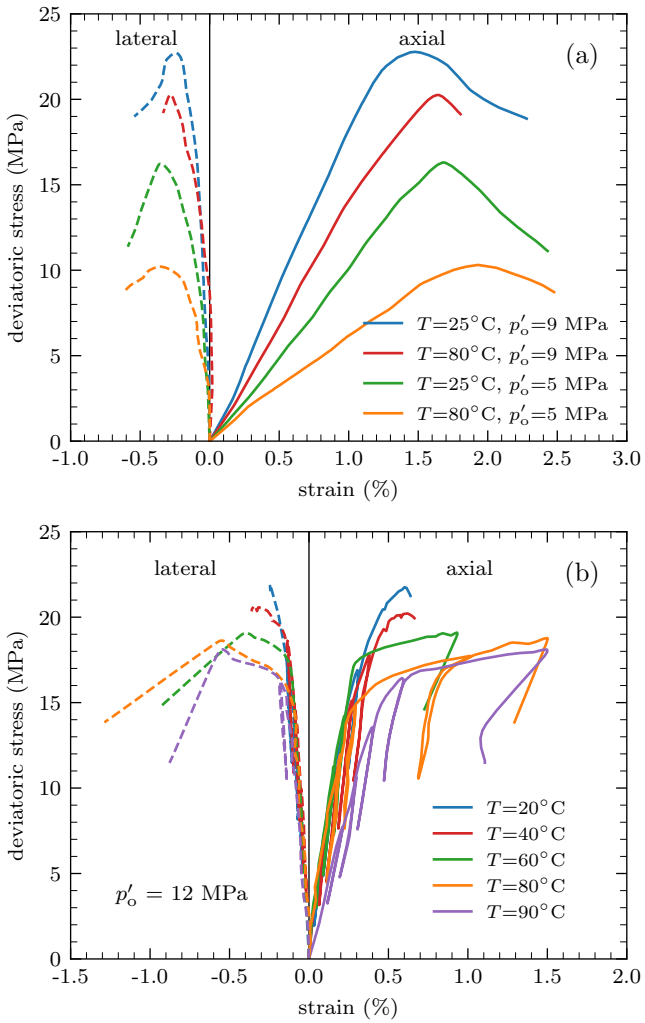

Figure 2: Results of drained (a) hollow cylinder triaxial tests (Menaceur et al., 2015) and (b) lateral decompression tests (Liu et al., 2019) on COx samples at different temperatures.

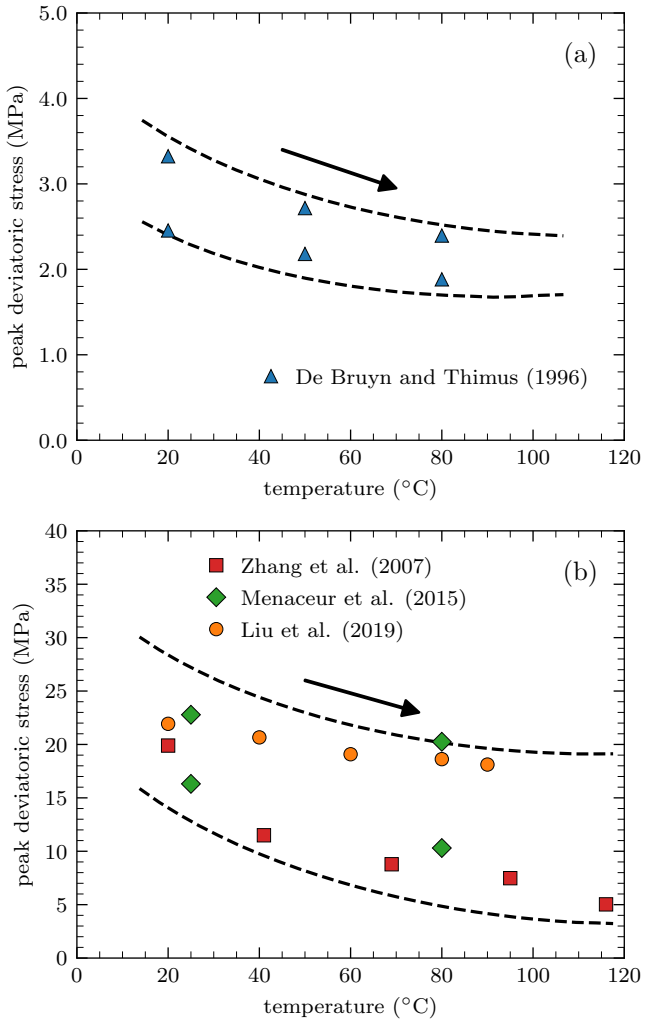

Figure 3: Evolution of peak strength with temperature for (a) Boom clay and (b) Opalinus clay and COx claystone samples.

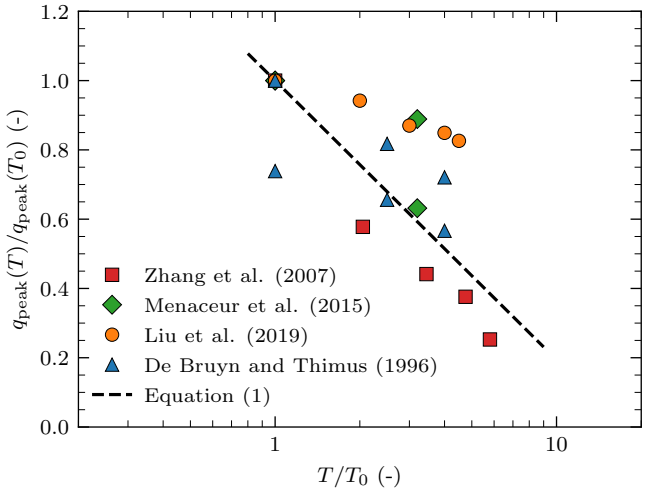

Figure 4: Normalised evolution of peak strength with temperature.

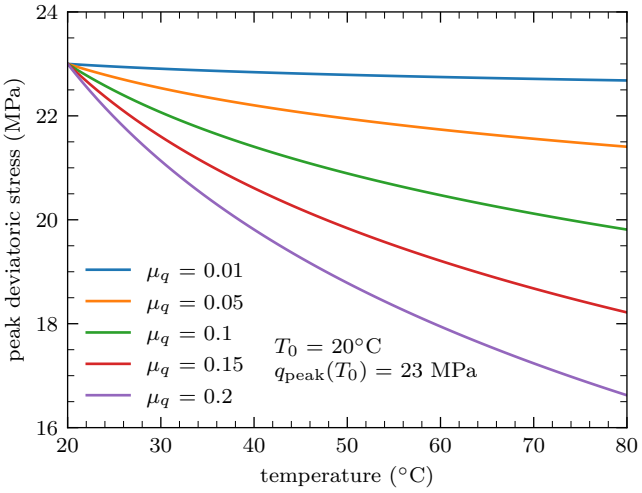

Figure 5: Variation of peak strength with temperature according to Equation 1, for different values of μ.

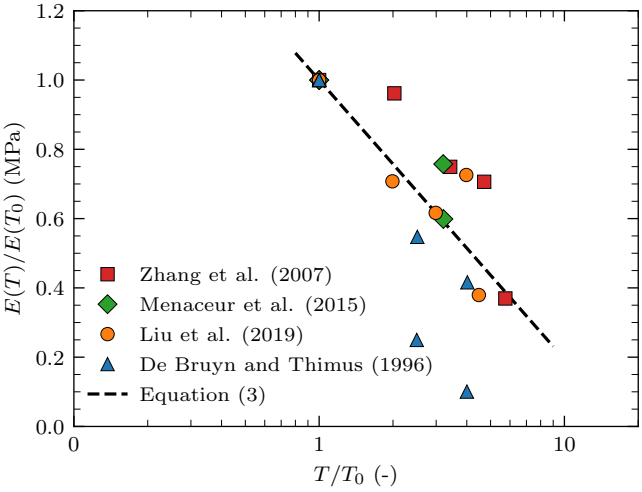

Figure 6: Normalised evolution of Young's modulus with temperature.

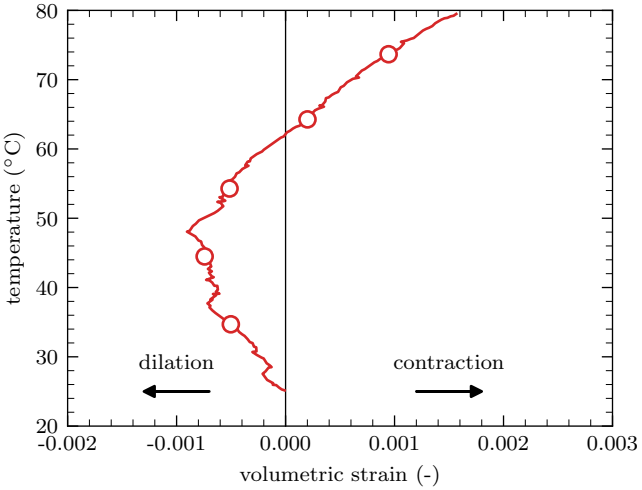

Figure 7: Thermally-induced volumetric strains in COx claystone samples (Belmokhtar et al., 2017).

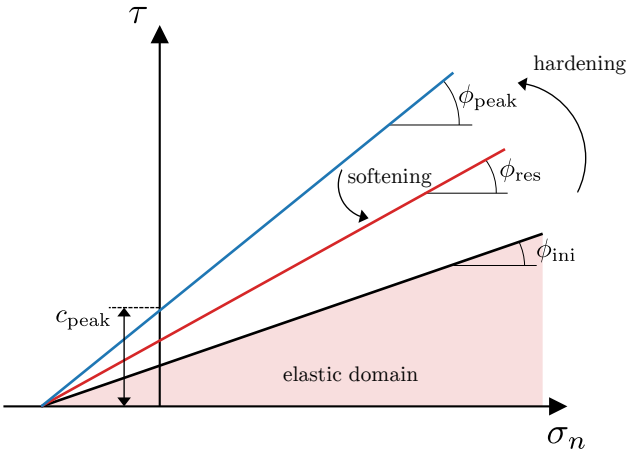

Figure 8: Evolution of the yield envelope.

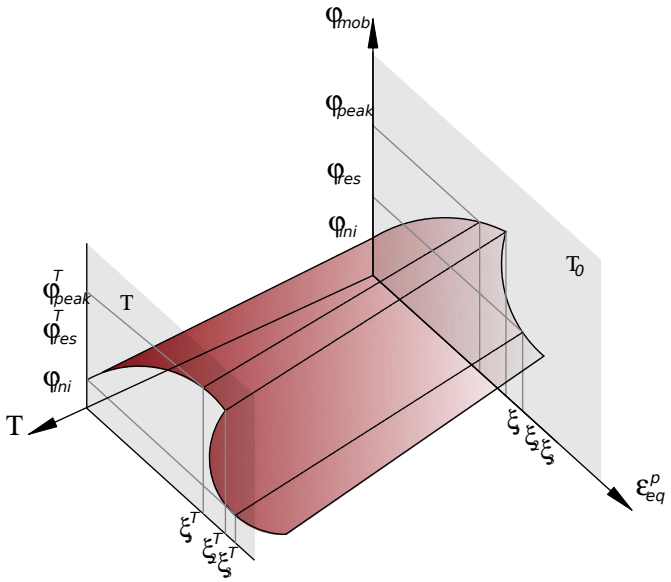

(a)

Figure 9: Mobilised friction angle as a function of temperature and $\boldsymbol{\epsilon}_{\mathrm{eq}}^{\mathrm{p}}$.

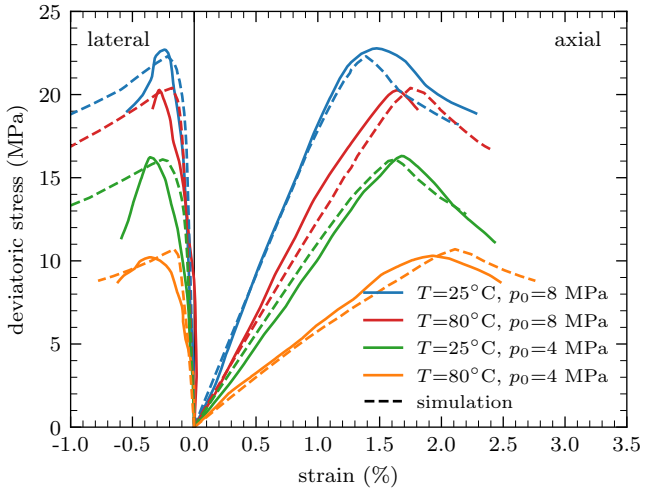

Figure 10: Drained hollow cylinder triaxial tests from (Menaceur et al., 2015) and simulation results.

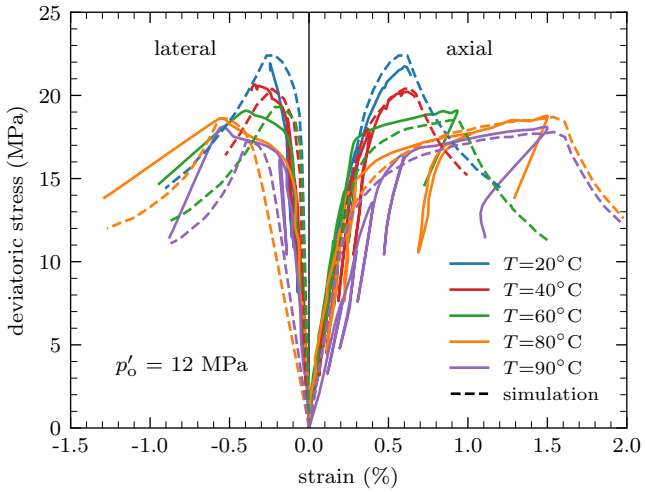

Figure 11: Triaxial lateral decompression tests from Liu et al. (2019) and simulation results.

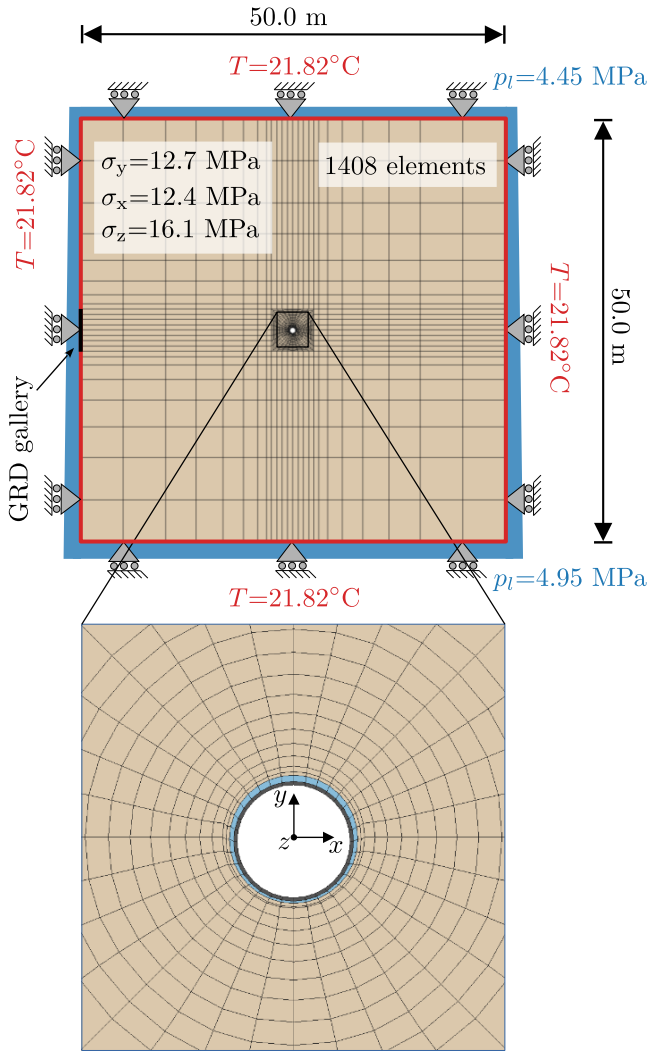

Figure 12: Model geometry, boundary conditions and finite element mesh employed (Tourchi et al., 2020).

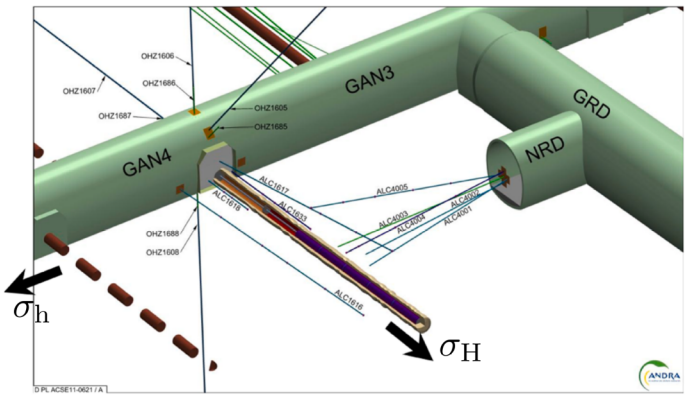

Figure 13: Schematic layout of the ALC1604 in situ heating tests (Bumbieler et al., 2021).

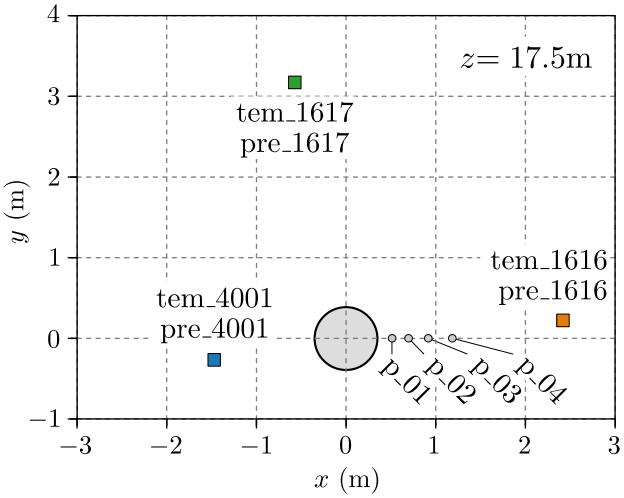

Figure 14: Location of the temperature and pore-water pressure measurement sensors used for comparison with simulation results.

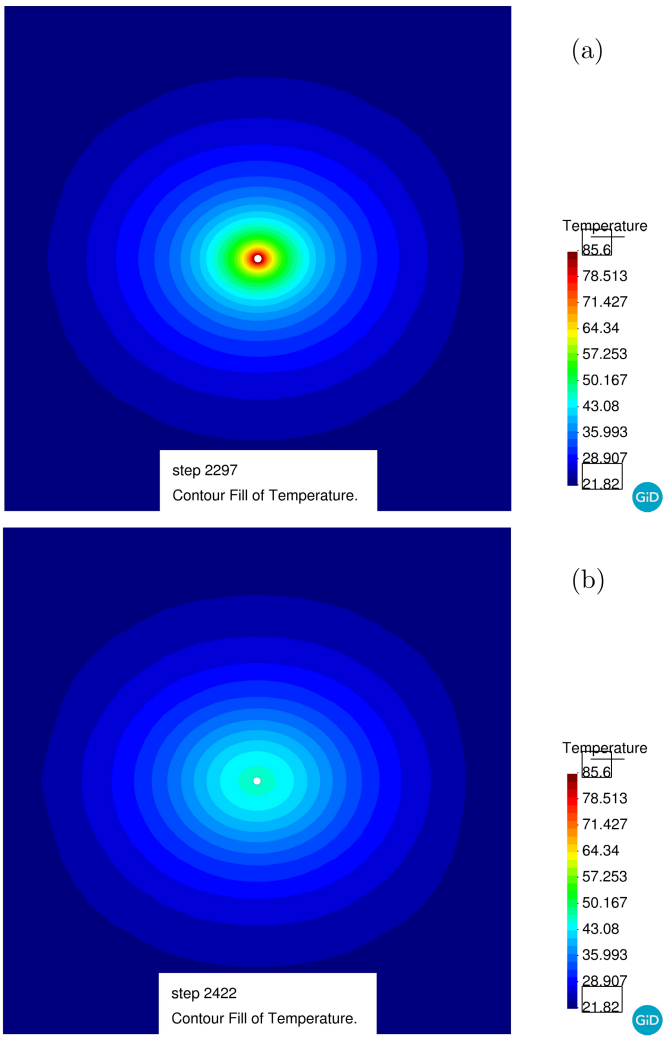

Figure 15: Computed contours of temperature (in °C) for (a) $t = 2297$ days (end of heating) and (b) $t = 2422$ days (end of second cooling phase).

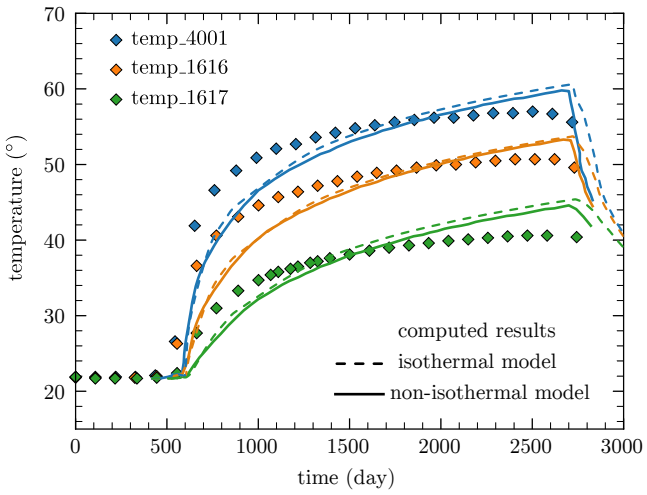

Figure 16: Observed and computed evolution of temperature at the observation points shown in Figure 14.

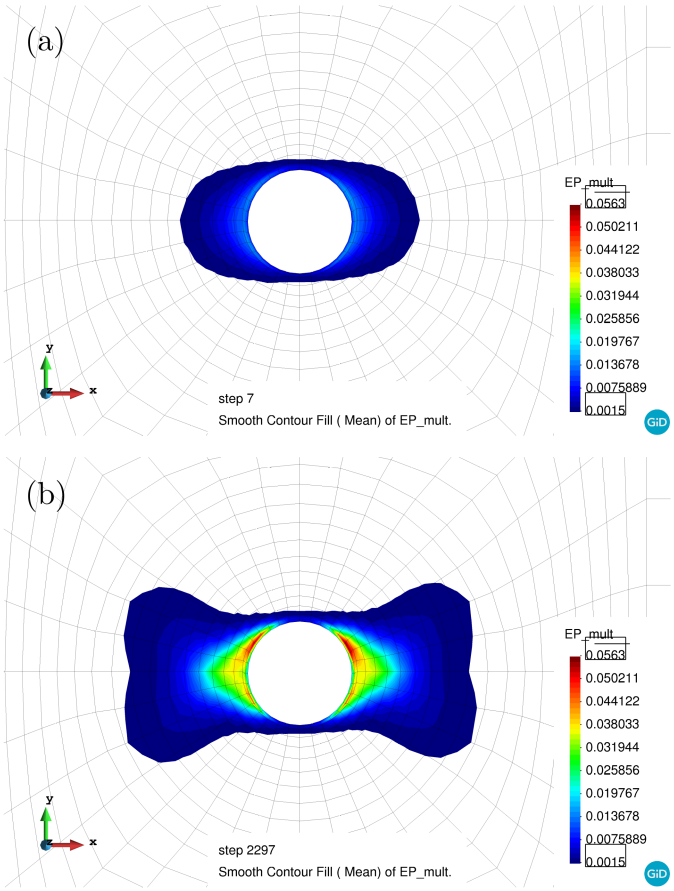

Figure 17: Obtained configuration of the EDZ in terms of contours of the plastic multiplier (a) after excavation and (b) at the end of the heating phase.

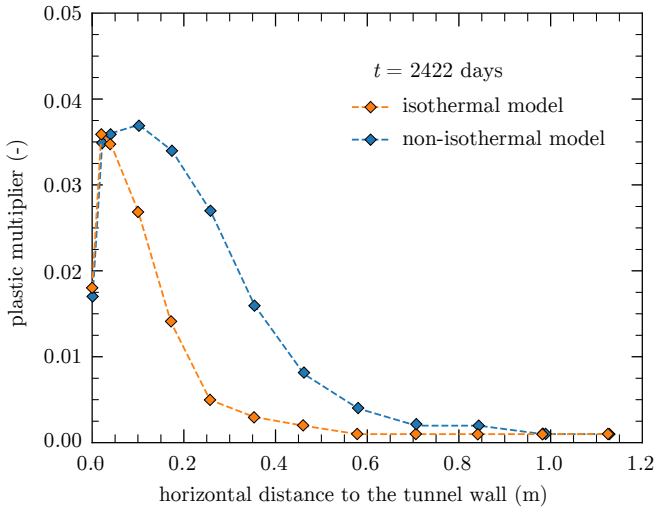

Figure 18: Computed plastic multiplier at the end of heating in the horizontal direction.

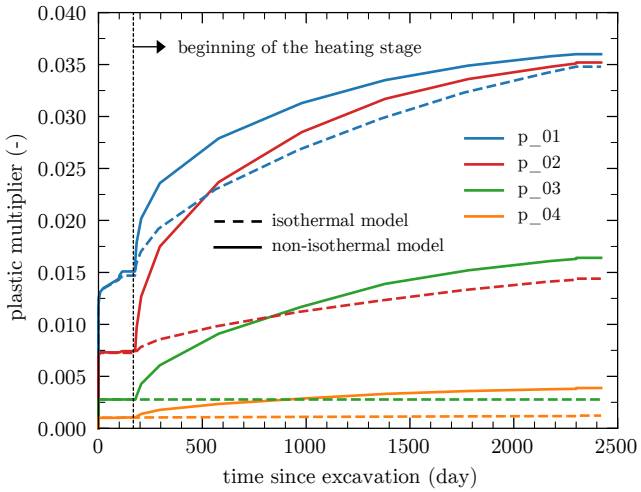

Figure 19: Computed plastic multiplier evolution at the observation points indicated in Figure 14.

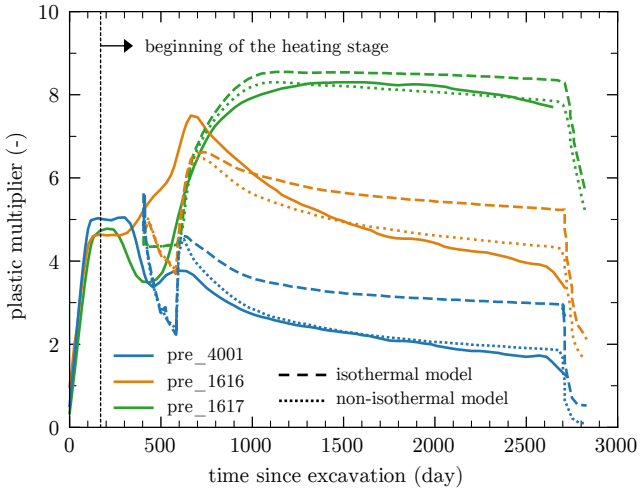

Figure 20: Computed pore-water pressure evolution at the observation points indicated in Figure 14.

Tables

Table 1: Model parameters adopted for the simulation of the triaxial tests from Menaceur et al. (2015) and the lateral decompression tests from Liu et al. (2019) with temperature control.

Parameter	Units	Triaxial	Decompression
E	(MPa)	1200*, 2000**	6000
ν	(-)	0.1	0.1
$\phi_{\text{ini}}^{T_0}$	(°)	9.35	9.35
$\phi_{\text{peak}}^{T_0}$	(°)	21.0	21.0
$\phi_{\text{res}}^{T_0}$	(°)	11.74	11.74
$c_{\text{peak}}^{T_0}$	(MPa)	3.5	3.5
a_{hard}	(-)	0.0035	0.0035
a_{soft}	(-)	0.07	0.07
ω	(-)	1.0	1.0
ξ_1	(-)	0.005	0.005
ξ_2	(-)	0.006	0.006
ξ_3	(-)	0.045	0.045
μ_ϕ	(-)	0.14	0.14
μ_E	(-)	0.275	0.07

*$p_0 = 5$MPa, **$p_0 = 9$MPa.

Table 2: Stages of ALC1604 in situ test.

Phase	Description	Start date	End date	Duration
1	Galleries GAN-GRD Excavation	9 September 2010	23 October 2012	775 days
2	Alveoli Excavation	23 October 2012	31 October 2012	8 days
3	Boreholes/Instrumentation	31 October 2012	30 January 2013	91 days
4	Heating Test (30W/m)	30 January 2013	15 February 2013	16 days
5	Cooling	15 February 2013	18 April 2013	62 days
6	Heating Stage (220W/m)	18 April 2013	6 February 2019	2120 days
7	First cooling phase (200W/m)	6 February 2019	8 April 2019	61 days
8	Second cooling phase (167W/m)	8 April 2019	11 June 2019	64 days

Table 3: COx properties used in the simulation (modified from Tourchi et al., 2021).

Parameter	Value
Hydraulic	
Parallel initial intrinsic permeability, $k_{0,xx}$ (m^2)	2.0E-20
Perpendicular initial intrinsic permeability, $k_{0,yy}$ (m^2)	1.0E-20
Parameter for the increase of k_0, η (-)	300
Parameter for the increase of k_0, λ_0 (-)	1.2E-4
Parameter in retention curve model, P (MPa)	14.3
Parameter in retention curve model, λ_r (-)	0.33
Parameter in the relative permeability model, A (-)	1.0
Parameter in the relative permeability model, Λ (-)	3.0
Hydro-mechanic	
Biot coefficient, b (-)	0.6
Thermal	
Parallel thermal conductivity, $k_{T,xx}$ (W m^{-1} K^{-1})	2.05
Parallel thermal conductivity, $k_{T,yy}$ (W m^{-1} K^{-1})	1.33
Specific heat capacity of the solid, c_s (J kg^{-1} K^{-1})	800
thermomechanical	
Linear thermal expansion coefficient of solids, α_s (K^{-1})	1.4E-5
Petrophysical	
Solid compressibility, β_s (Pa^{-1})	2.5E-5
Relative density, (-)	2.7
Porosity, Φ (-)	0.173
Normal scaling factor for anisotropy, C_N (-)	1.33
Shear scaling factor for anisotropy, C_S (-)	1.33
Rate of reduction of the stiffness with temperature, μ_E	0.27
Rate of reduction of the strength with temperature, μ_ϕ	0.37

Table 4: COx mechanical parameters for the thermomechanical reference model (modified from Tourchi et al., 2021).

Parameter	Value
Young's modulus, E_1 (MPa)	5200
Young's modulus, E_2 (MPa)	4000
Shear modulus, G_2 (MPa)	1480
Poisson's ratio, ν_1 (-)	0.25
Poisson's ratio, ν_2 (-)	0.35
Initial friction angle, $\phi_{\text{ini}}^{T_0}$ (°)	9.35
Peak friction angle, $\phi_{\text{peak}}^{T_0}$ (°)	22.0
Residual friction angle, $\phi_{\text{residual}}^{T_0}$ (°)	14.74
Peak cohesion, $c_{\text{peak}}^{T_0}$ (MPa)	3.55
Parameter controlling hardening, a_{hard}, (-)	0.0035
Parameter controlling softening, a_{soft}, (-)	0.07
Parameter in the flow rule, ω, (-)	1.0
The value of $\epsilon_{\text{eq}}^{\text{p}}$ at peak strength, ξ_1 (-)	0.005
Threshold for viscoplastic strains, σ_s, (MPa)	4.0
Viscosity parameters, γ (day^{-1})	1.0E-7
Parameter in the time-dependent component, n	3.37
Parameter in the time-dependent component, m	530

Table 5: Parameters adopted for the steel casing (modified from Tourchi et al., 2021).

Parameter	Value
Mechanical	
Young's modulus, E (GPa)	210.0
Poisson's ratio, ν,	0.3
Thermal	
Thermal conductivity, k_T (W m^{-1} K^{-1})	80
Specific heat capacity of the solid, c_s (J kg^{-1} K^{-1})	800
Linear thermal expansion coefficient of solids, α_s (K^{-1})	1.4E-5

Table 6: Parameters adopted for the annular space (modified from Tourchi et al., 2021).

Parameter	Value
Mechanical	
Young's modulus, E_{open} (MPa)	10.0
Young's modulus, E_{closed} (MPa)	1000.0
Poisson's ratio, ν (-)	0.3
Volumetric strain for gap closure, $\epsilon_{v,\text{limit}}$	0.005
Thermal	
Thermal conductivity, $k_{T,\text{dry}}$ (W m^{-1} K^{-1})	0.35
Thermal conductivity, $k_{T,\text{sat}}$ (W m^{-1} K^{-1})	0.6
Hydraulic	
Intrinsic permeability, k_0 (m^2)	2.0E-20
Parameter in retention curve model, P (MPa)	14.3
Parameter in retention curve model, M (-)	0.33